Nanoscale

Accepted Manuscript

Graphical Abstact

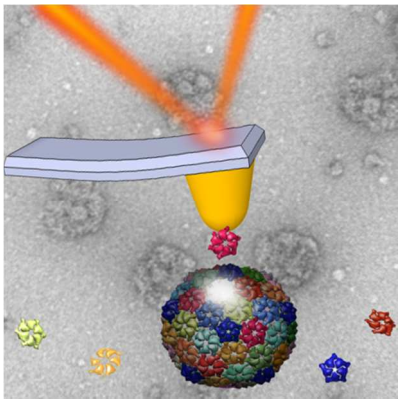

The association of stability and stiffness may be a false friend for viral cages. We found that two kind of particles with similar stiffness present different stability under aggressive environments. Fracture analysis and coarse grained simulations provide a correct interpretation of virus mechanics in terms of stability.

The interplay between mechanics and stability of viral cages

Mercedes Hernando-Pérez[a], Elena Pascual[b], María Aznar[c], Alina Ionel[b], José R. Castón[b], Antoni Luque[d], José L. Carrascosa[b], David Reguera[c] and Pedro J. de Pablo[a]

Abstract

The stability and strength of viral nanoparticles are crucial to fulfill the functions required through the viral cycle as well as using capsids for biomedical and nanotechnological applications. Mechanical properties of viral shells obtained through Atomic Force Microscopy (AFM) and continuum elasticity theory, such as stiffness or Young´s modulus, have been interpreted very often in terms of stability. However, viruses are normally subjected to chemical rather than to mechanical aggressions. Thus, a correct interpretation of mechanics in terms of stability requires an adequate linkage between the abilities of viral cages to support chemical and mechanical stresses. Here we study the mechanical fragility and chemical stability of bacteriophage T7 in two different maturation states: the early proheads and the final mature capsids. Using chemical stress experiments we show that proheads are less stable than final mature capsids. Still, both particles present similar anisotropic stiffness, indicating that a continuum elasticity description in terms of Young's modulus is not an adequate measure of viral stability. In combination with a computational coarse-grained model we demonstrate that mechanical anisotropy of T7 emerges of the discrete nature of the prohead and empty capsid. Even though they present the same stiffness, proheads break earlier and have fractures ten times larger than mature capsids, in agreement with chemical stability, thus demonstrating that fragility rather than stiffness is a better indicator of viral cages stability.

Introduction

Viruses are nanoscopic nucleoprotein complexes optimized through evolution to efficiently replicate their genome and transfer from host to host. The viral genetic material is stored in a protein cage, called the capsid. The viral capsid assembly usually requires a complex maturation pathway, where a cascade of structural changes tunes its morphology and strength to properly set the delivery mechanism for the genome. This process guarantees not only the infectivity of the viral particles [1], but also their stability during the extracellular cycle. Viruses face a variety of physicochemical environmental conditions [2], such as extremes of temperature and pH, osmotic shocks [3] or dehydration [4]. Hence, the capsid maturation endorses viruses with physical properties that are essential for their infection cycle and survival. In the last years Atomic Force Microscopy (AFM) [5] has facilitated to study a variety of physical properties of viral cages, ranging from their high elasticity to the mechanical buttressing supplied by the nucleic acids [6-9], including the influence of defects on shell stiffness [10], and built-in stress reinforcement phenomena [11, 12]. AFM nanoindentation experiments enable to derive their effective Young´s modulus [13] by measuring their stiffness and considering viral shells as homogeneous and continuous structures, either using Finite Element Analysis [14] or analytical continuum models [15, 16]. Hence stiffness [10] and Young's modulus [16] of viral particles have been directly associated to capsid stability. However, during the extracellular cycle viruses confront chemical rather than mechanical aggressions. Thus the stability of a virus might not be strictly related to its Young's modulus or stiffness.

We have worked with bacteriophage T7, which has an icosahedral capsid with a short non-contractile tail[17]. T7 first assembles into the prohead, which is a shell built by 415 copies of the structural protein gp10A arranged in a T=7 icosahedral lattice[17]. The proteins are distributed in clusters of 6 (hexons) and 5 (pentons) subunits. The shell contains a dodecameric connector (gp8) at one five-fold vertice, which is linked to an inner cylinder-like core (gp14, 15 and 16) essential for infectivity [18]. Between the core and the shell there is a scaffold of multiple copies of a single protein, which is instrumental for the prohead assembly. The T7 capsid maturation process involves the packaging of 40 kb of double-stranded (ds) DNA into the prohead, the release of the scaffold, the expansion of the shell, and the incorporation of the tail proteins in the connector vertex[17]. The non-contractile tail of 18.5 nm in length assembles into the same capsid vertex where the connector is located[19]. The drastic changes within the maturation process involve a diameter increment from 51 to 60 nm, with an associated shell thinning from 4.1 to 2.3 nm (Fig. 1)[17 20], and entail an extensive reorganization of the interactions among all shell protein subunits [21].

Here we investigate the phenomenological correlation between the mechanical and chemical resistances of emptied bacteriophage T7 particles. While proheads are less stable than capsids upon chemical treatment, both particles have the same anisotropic stiffness that is incompatible with continuum elastic theory. Thus, we utilize cycling load to quantify the mechanical fragility of viral shells by inducing single capsomer fractures. We rationalize the mechanical properties of T7 using a coarse-grained model that captures the discrete nature of the shell.

Results

Chemical stability of bacteriophage T7 capsids

To test the chemical stability of T7 particles we used urea and guanidinium hydrochloride (GuHCl), two standard reagents for protein denaturing studies. Whereas urea mainly disrupts hydrophobic interactions leading to unfolding and eventual denaturation of proteins, GuHCl preferentially weakens electrostatic interactions by masking charged residues [21-23]. Purified T7 proheads and mature, tail-less, DNA empty capsids were incubated with different concentrations of urea and GuHCl (Materials and Methods, M&M). Fig. 1c shows a representative gallery of images obtained after such treatments. T7 proheads disrupted after incubation in 3M urea for 20 min, and they were completely disassembled in 4M urea; they also followed a similar behavior after incubation in 1-2 M GuHCl. In contrast, T7 mature capsids withstanded extended incubations with both urea and GuHCl. Thus, the maturation process increases the structural stability of bacteriophage T7 against chemical treatments. This increased endurance would provide bacteriophages with the capability of standing in the hostile conditions during their extracellular cycle.

Stiffness measurements of T7 particles

To find a phenomenological link between chemical and mechanical stabilities, we studied several mechanical properties of proheads and mature capsids with Atomic Force Microscopy (AFM) in liquid milieu. The adsorption geometries of T7 particles on the substrate were first identified (Fig. 2). AFM prohead images are consistent with the 5-fold and 3-fold symmetries axes (Fig. 2a, c) in 23% and 26% of the cases, respectively. However, 51% of prohead particles appeared tilted with adsorption geometry undetermined, and these particles were termed as non-specific orientation (NSO) particles (Fig. 2e). For T7 mature capsids, 2-fold, 3-fold, and 5-fold orientations were identified in 12%, 31%, and 31% of 41 particles, respectively (Fig. 2). Only 26% of the capsids were NSO particles. Interestingly the adsorption symmetry ratio of both proheads and mature capsids is different from the one expected for an icosahedron that binds to the surface with equal probability through all symmetries [24] (30:20:12 for the 2-fold, 3-fold, and 5-fold orientations, respectively). The high occurrence of the adsorption through the 3-fold symmetry axis reveals that the capsid binding to the surface is dominated by the area of contact between the shell and substrate. Our high resolution AFM images resolved the hexons and pentons of T7 (Fig. 2f), as well as the height of the particles (50-60 nm) that matched the dimensions derived from cryo-Electron Microscopy (cryo-EM) studies, implying that no significant deformation is induced upon adsorption on the surface.

The initial mechanical characterization consisted on nanoindentation experiments on both proheads and capsids keeping the maximum force low enough to avoid nonlinearities and steps. From the linear regime, we extracted their elasticity as a function of the different geometrical orientations, including NSO particles (Supplementary Information, SI, Fig. S1). Single indentation assay experiments on proheads consisted on 137 nanoindentations performed on 3-fold (7 particles), 5-fold (8 particles) and NSO (10 particles) symmetry axis. The spring constants (Fig. 2g, red) were k^P_3 =0.24±0.04 N/m, k^P_5 =0.10±0.02 N/m and k^P_{NSO} =0.17±0.04 N/m for 3-fold, 5-fold and NSO, respectively (Table 1). For mature capsids we performed 219 nanoindentations on 2-fold (5 particles), 3-fold (13 particles), 5-fold (13 particles) and NSO (10 particles) symmetry axes. The capsid spring constants (Fig. 2g, grey) resulted in k^C_2 =0.40±0.02N/m, k^C_3 =0.21±0.03 N/m, k^C_5 =0.11 ± 0.02 N/m and k^C_{NSO} =0.17 ±0.04 N/m for 2-fold,

3-fold, 5-fold and NSO adsorption geometries, respectively (Fig. S1). These results show that both T7 proheads and mature capsids have a similar anisotropic elastic response. In contrast with the different behaviour observed for both types of particles under chemical stress, bacteriophage T7 capsid rigidity does not vary upon maturation [9].

Finite element analysis

To understand the origin of the anisotropic elastic response of T7 and obtain its Young´s modulus, we implemented finite element (FE) models of increasing levels of complexity (SI). Our AFM experiments showed that the icosahedral spring constants of T7 capsids follow the relation $k_5<k_3<k_2$. Nevertheless, for a homogeneous thin shell icosahedral model, the stiffness obtained in FE simulations is $k_5<k_2<k_3$ along with the increased thickness [6]. Finite element simulations of a *thick* icosahedral shell with the same dimensions as T7 (Fig. S2) also predict an incorrect order of the elastic constants ($k_2<k_3<k_5$), as shown in Fig. S3. In addition we used a 3D topographically detailed mesh [25], based on the lattice derived from the cryo-EM volume [26] to model an inhomogeneous finite element capsid [25] (Fig. S4) yielding an ordering of stiffness ($k_2\approx k_3<k_5$, SI Fig. S5), that is again in disagreement with the experimental findings. Therefore, the experimental mechanical response of T7 is not reflected in the framework of continuum elasticity, and Young´s modulus cannot be computed.

Nanoindentation simulations of a discrete model of T7 virus

Previous coarse-grained models of viral capsids have shown that the discrete nature of the viral shell has a significant influence in the mechanical properties, especially for small viruses [27-29].

Accordingly, we also further explored whether the discrete nature of the viral shell is responsible for the observed experimental results. First, we estimated the shell stiffness from structural data [26] calculating the total surface of the inter-capsomer contacts involved in the local deformation, which depends on the orientation of the viral capsid (SI). Using this approach (Fig. S6), we obtained that the 3-fold and 2-fold axes are around 2 and 3 times stiffer, respectively, than the 5-fold axis. This is in good agreement with the AFM experiments, where the indentations for the 3-fold and 2-fold axes result in spring constants that are 2 and 4 times larger, respectively, than for the 5-fold case (Table S1).

To corroborate that discrete effects dominate the mechanical response of the T7 capsid, as suggested by previous models [27-29], we have also performed virtual AFM simulations for a discrete model of the bacteriophage T7 capsid, coarse-grained at the level of the morphological units (capsomers) [26] (SI). Fig. 3a shows a snapshot of the virtual AFM simulations and Fig. 3b the resulting indentation curves. Remarkably, this discrete model reproduces the same order of the effective spring constants found in the experiments, $k_5<k_3<k_2$ (Fig. 3c).

Mechanical fatigue and fracturing of T7 particles

Since neither the elasticity nor the Young's modulus resembles the chemical stability upon maturation, we devised alternative experimental approaches for studying mechanical stability. Mechanical fatigue is commonly used to check the stability of macroscopic samples [30], and it has also been applied to nanometric viral structures, where an individual particle is subjected to a repeated cycling load at low forces [31]. However, we have found that imaging forces of a few hundreds pN do not affect phage T7 stability. Thus, we designed an intermediate approach between the classical indentation assays and the mechanical fatigue experiments. In our new procedure we performed a series of individual controlled indentations that deform the viral particles about three times the shell thickness during the linear regime, i.e., ~6 nm. This deformation is gentle enough to avoid the complete demolition of the particle in a single indentation [32], but it is sufficiently strong to eventually lead to the virus fracture. The particle is imaged after each indentation to check its topographical integrity. We applied this methodology to both proheads and mature capsids. As an illustrative case, Fig. 4a shows an intact prohead oriented along a 5-fold symmetry axis. After two consecutive indentations (Fig. 4b, grey lines), the prohead remained unaltered, but the third one (Fig. 4b, red line) induced a crack (Fig. 4c). Alternatively, Fig. 4d presents a NSO prohead symmetry axis that broke after one load cycle (Fig. 4e), and the crack extended over the center of the shell (Fig. 4f).

Similar fatigue experiments with mature capsids showed that the particle adsorbed along a three-fold symmetry axis (Fig. 5a1) remained unaltered until the 9th indentation (Fig. 5a2, red line) when the first overall topographical change is observed (Fig. 5a3). Filtered topographies (Experimental Section) of the damaged region before (Fig. 5a4) and after breakage (Fig. 5a5) suggested that one hexon of the triangular facet lost one monomer, as depicted in Fig. 5a6. To support this hypothesis, we generated a geometrical tip-dilated structure [33, 34] using the EM T7 capsid volume [26] with the absence of a monomer. When compared with the AFM images, the model showed that the observed damage most likely corresponds to a single monomer vacant (Fig. S7). In another experiment on a three-fold axis of a capsid (Fig. 5b1), the fourth load cycle (Fig. 5b2, red line) induced a crack that probably corresponds to a missing trimer (Fig. 5). Likewise, Fig. 5c presents the case of a 5-fold oriented particle that releases a penton at the third indentation.

Another mechanical parameter typically measured in AFM experiments is the breaking force, which is associated to sudden drops in the force-indentation curves. However, the assignation of a breaking force using this protocol is ambiguous because the drop in the force can be related to reversible buckling events [14, 35], sliding or rotation of the particle, temporal breakages, or non-detectable protein bond changes. Our data, for instance, present several sequential decreases in load cycles that do not induce any apparent topographic damage (Fig. 5a2, 5b2, 5c2; grey lines). Thus, particles should routinely be imaged after the indentation to certify and characterize any change in the structure. First, we quantified the damages of viral capsids by measuring the depths of the cracks. We compared the topographical profiles between the intact and fractured proheads (Fig. 4c, 4f, insets; Fig. S8), observing cracks from 10 to 24 nm in depth. In contrast, on capsids the same analysis showed shallower depths from 1.6 to 7.0 nm (Fig. 5a3, 5b3 and 5c3; insets, Fig. S9). In addition, the crack areas are also larger in proheads than in mature capsids. In order to make a more quantitative assessment of the fragility of the particles, we calculated the amount of removed material after cracking by subtracting the topography of the damaged virus from

the intact one. This approach simultaneously provided the volume and area lost in fractured proheads (Fig. S8) and capsids (Fig. S9). Fig. 6a presents the ratios of the removed (ΔA, ΔV) and the original areas and volumes (A, V) for 8 proheads (red) and 10 capsids (black) subjected to consecutive load cycles. Proheads lose significantly more material than capsids, as indicated by the higher ratios of lost area and volume, which in proheads, respect to the capsids, are one order of magnitude larger.

Remarkably we have observed a linear behavior in the log-log plot for the removed volume and area with a slope of 1.57±0.06 (inset, Fig. 6a). This behavior excellently matched with the scaling dependence expected between these two magnitudes, $\Delta V \propto \Delta A^{3/2}$, proving the consistency an accuracy of our breakage experiments. Finally, the number of load cycles needed to fracture a particle also provided crucial information about their stability. Fig. 6b depicts the area ratio of each crack ΔA/A, vs. the associated number of load cycles. This graph shows that proheads develop larger fractures in a few indentations compared to capsids, which tolerate more cycles until they eventually fracture forming much smaller cracks.

Discussion

We have found that the anisotropic elastic response of T7 viral capsids obtained from AFM indentation experiments does not follow the anisotropy expected from continuum homogenous models [5]. Using a coarse-grained simulation for the nanoindentation of T7 capsids, we have shown that the anisotropic elastic response stems from the discrete nature imposed by the structural units of the capsid and their precise arrangement on the viral shell.

Previous structural studies of the T7 capsid showed that intra-capsomer interactions are stronger than inter-capsomer interactions [26], which is consistent with our discrete model using single block capsomers. The origin of the stiffness anisotropy is important for deriving mechanical parameters that should be crucial for the interpretation of bacteriophage T7 stability. Thin shell theory, for instance, has been thoroughly used to calculate Young's modulus of viral shells [5]. In the case of homogeneous materials, this approximation works fairly well. However, the anisotropy of the stiffness in bacteriophage T7 would provide multiple values for Young's modulus which is inconsistent with a homogeneous material framework. Thus, Young's modulus is inappropriate to characterize the mechanical response or stability of T7 [16] and it might not be accurate in other cases due to the inhomogeneous and discrete nature of the viral structures.

In contrast, the quantification of the ruptures induced by sequential load unveils clear differences between the stability of proheads and capsids. Specifically, whereas prohead loses upon breakage 48 ± 15 % (average ± SD) and 7 ± 2% of its projected area and volume, respectively, a capsid loses only about 5 ± 3% area and 0.2 ± 0.1% of volume (Table S2). In addition, high resolution AFM topographies of proheads reveal a massive cracking involving several capsomers, mostly corresponding to the pyramidal footprint left by the tip shape (Fig. 4 and Fig. S8). Distinctly the topographies of broken capsids show ruptures associated to individual subunits, such as monomers, trimers, and individual capsomers (Fig. 5 and Fig. S9). Interestingly, the calculation of the normalized area corresponding to monomer, trimer and capsomer vacants underestimate the corresponding experimental values (arrows of inset, Fig 6a), since it does not consider deformations of the fracture. Moreover, our fatigue experiments demonstrate that after four load cycles only about 20% of capsids are damaged, whereas 90% of proheads are already broken. The increase of contact areas among capsomers generated during maturation together with the

reinforcement by the molecular swapping of the contacts around the 3-fold symmetry axes [21] not only enhances the particles viability on chemically severe conditions, but also increases their resistance against fracture. Thus, maturation increases the mechanical stability of viral particles against fracture as well as their chemical stability against urea and GuHCl assaults, but not their stiffness. Hence, fragility against fracture is a more appropriate indicator of stability than elasticity or Young's modulus.

Experimental

Chemical treatment of T7 particles

T7 proheads and empty mature heads, purified as described in Supplemantary Information, were incubated with different concentrations of urea (Merck) or guanidine hydrochloride (Sigma Life Science) in TMS. Samples were taken after 60 min incubation at room temperature, dialyzed against TMS and prepared for transmission electron microscopy. The samples were adhered to carbon-coated grids, negatively stained with 2% uranyl acetate, and imaged in a Jeol 120EX microscope.

AFM experiments on viral particles

Stocks of T7 viral particles were stored in TMS buffer (10 mM MgCl2, 50 mM Tris and 100 mM NaCl, pH 7.8). A drop of 20 µl stock solution of viral particles was left on HOPG (ZYA quality NTMDT), for 30 min and washed with buffer. The tip was prewetted with 20 µl of buffer. The AFM (Nanotec Electrónica S.L., Madrid, Spain) was operated in jumping mode in liquid [36] using rectangular cantilevers RC800PSA, and (Olympus, Tokyo, Japan) with nominal spring constants of 0.05 N/m. Cantilevers spring constants were routinely calibrated by using the Sader's method [37]. To determine the stiffness of proheads and empty capsids, once individual particles were located on the surface, the lateral piezo scan was stopped when the tip was on top of the particle. Then, force-vs.-distance curves were obtained by elongating the z-piezo until the tip established mechanical contact with the viral particle. The viral particle is indented with a few separate sets of FZs of more than 5 indentations in each one. The FZ speed is about 50 nm/s [38]. In our experiments only particles showing stable spring constants along the FZs sets were considered to avoid particle mobility effects that often occur when the particle is loosely bound to the surface. During the first stages of indentation the viral particles show a linear deformation [39] which provides the spring constant of the virus k_v (if it is considered like a spring in series with the cantilever) as $k_v = k_c \frac{S_g}{S_v - S_g}$, where k_c is the spring constant of the cantilever, S_g (nm/V) the slope of the cantilever deflection on the glass (the substrate is considered as non-deformable) and Sv (nm/V) the slope of the cantilever deflection on the virus. In the experiments targeted on obtaining the spring constant, the force curves reached maximum indentations of the thickness of the T7 shell, i.e., between 2 and 2.5 nm (Fig. S1). Load cycles experiments were performed by consecutively deforming the particles about 6 nm. After each indentation, every particle is imaged to verify any topographical change. This methodology is used until the first damage is detected. Undesired rotations and displacements of particles occurred often during these experiments, thus only about 25% of the targeted particles were stable enough.

AFM images and tip-dilated EM models were processed and generated by using WSxM software [34]. The filtered methodology of Figs S5, S8 and S9 consisted on removing the curvature of the virus from the topographical data.

Conclusion

In summary, we have studied the stability of T7 particles upon maturation under chemical and mechanical stress. Chemical treatment of viral particles with urea and GuHCl has shown that maturation increases their stability. The elastic response of both proheads and capsids is anisotropic and not compatible with continuum elasticity theory. The origin of this anisotropy is the discrete and non-homogeneous nature of the viral shell, as demonstrated with AFM coarse-grained simulations of the capsid. Remarkably, the increased chemical resilience of capsids versus proheads observed upon maturation is not accompanied by an increase of stiffness, which in this case is not a proper measure of viral stability. Instead, our controlled fatigue experiments reveal that the fracture size of proheads is about ten times larger than the capsid one. Consecutive load cycles induce large fractures on proheads after a few indentations, whereas in mature shells the fracture occurs after many cycles and only involves a limited number of protein subunits. Our quantitative analysis of the strength and integrity of shells in the maturation of T7 establishes a phenomenological link between fragility and chemical stability in viral capsids.

Acknowledgments

We acknowledge funding by grants from the Ministry of Science and Innovation of Spain, PIB2010US-00233, FIS2011-29493 and Consolider CSD2010-00024 (to P.J.P.), FIS2011-22603 and FIS2011-16090-E (D.R), BFU2011-29038 (to J.L.C.), BFU2011-25902 (to J.R.C.) and the Comunidad de Madrid No. S2009/MAT-1467 (to P. J. P) and S2009/MAT-1507 (to J.L.C.) We are grateful to M. García-Mateu (UAM), Julio Gómez-Herrero (UAM) and Red Española Interdisciplinar de Biofísica de los Virus (BioFiViNet), FIS2011-16090-E for expert technical help.

Note and References

[a]Departamento de Física de la Materia Condensada C03, Universidad Autónoma de Madrid, 28049 Madrid, Spain.

[b]Department. Structure of Macromolecules, Centro Nacional de Biotecnología/CSIC, Cantoblanco, 28049 Madrid, Spain.

[c]Departament de Física Fonamental, Facultat de Física, Universitat de Barcelona, Martí i Franquès 1, 08028 Barcelona, Spain.

[d]Department of Chemistry, New York University, 100 Washington Square East, New York, NY 10003, USA.

Electronic Supplementary Information (ESI) available: Purification of T7 proheads and capsid, Coarse-Grained simulations of the indentation of T7 empty capsids, Finite Element (FE) simulations, and Justification of the anisotropic stiffness based on structural information. See DOI: 10.1039/b000000x/

1. S. J. Flint, L. W. Enquist, V. R. Racaniello and A. M. Skalka, *Principles of virology*, ASM Press, Washington D.C., 2004.
2. M. F. Moody, *Journal of Molecular Biology*, 1999, **293**, 401-433.
3. A. Cordova, M. Deserno, W. M. Gelbart and A. Ben-Shaul, *Biophys. J.*, 2003, **85**, 70-74.
4. C. Carrasco, M. Douas, R. Miranda, M. Castellanos, P. A. Serena, J. L. Carrascosa, M. G. Mateu, M. I. Marques and P. J. de Pablo, *Proc. Natl. Acad. Sci. U. S. A.*, 2009, **106**, 5475-5480.
5. I. L. Ivanovska, P. J. C. Pablo, B. Ibarra, G. Sgalari, F. C. MacKintosh, J. L. Carrascosa, C. F. Schmidt and G. J. L. Wuite, *Proc. Natl. Acad. Sci. U. S. A.*, 2004, **101**, 7600-7605.
6. C. Carrasco, A. Carreira, I. A. T. Schaap, P. A. Serena, J. Gomez-Herrero, M. G. Mateu and P. J. Pablo, *Proc. Natl. Acad. Sci. U. S. A.*, 2006, **103**, 13706-13711.
7. C. Carrasco, M. Castellanos, P. J. de Pablo and M. G. Mateu, *Proc. Natl. Acad. Sci. U. S. A.*, 2008, **105**, 4150-4155.
8. I. Ivanovska, G. Wuite, B. Jonsson and A. Evilevitch, *Proc. Natl. Acad. Sci. U. S. A.*, 2007, **104**, 9603-9608.
9. M. Hernando-Pérez, R. Miranda, M. Aznar, J. L. Carrascosa, I. A. T. Schaap, D. Reguera and P. J. de Pablo, *Small*, 2012, **8**, 2365.
10. W. H. Roos, K. Radtke, E. Kniesmeijer, H. Geertsema, B. Sodeik and G. J. L. Wuite, *Proceedings of the National Academy of Sciences of the United States of America*, 2009, **106**, 9673-9678.
11. C. Carrasco, A. Luque, M. Hernando-Perez, R. Miranda, J. L. Carrascosa, P. A. Serena, M. de Ridder, A. Raman, J. Gomez-Herrero, I. A. T. Schaap, D. Reguera and P. J. de Pablo, *Biophysical Journal*, 2011, **100**, 1100-1108.
12. M. Baclayon, G. K. Shoemaker, C. Uetrecht, S. E. Crawford, M. K. Estes, B. V. V. Prasad, A. J. R. Heck, G. J. L. Wuite and W. H. Roos, *Nano Letters*, 2011, **11**, 4865-4869.
13. W. H. Roos, R. Bruinsma and G. J. L. Wuite, *Nature Physics*, 2010, **6**, 733-743.
14. W. S. Klug, R. F. Bruinsma, J. P. Michel, C. M. Knobler, I. L. Ivanovska, C. F. Schmidt and G. J. L. Wuite, *Phys. Rev. Lett.*, 2006, **97**, 228101.
15. L. D. Landau and E. Lifshizt, *Theory of Elasticity*, Pergamon London, 1986.
16. W. H. Roos, I. Gertsman, E. R. May, C. L. Brooks, J. E. Johnson and G. J. L. Wuite, *Proc. Natl. Acad. Sci. U. S. A.*, 2012, **109**, 2342-2347.
17. X. Agirrezabala, J. Martin-Benito, J. R. Caston, R. Miranda, M. Valpuesta and J. L. Carrascosa, *Embo Journal*, 2005, **24**, 3820-3829.
18. L. R. Garcia and I. J. Molineux, *Journal of Bacteriology*, 1996, **178**, 6921-6929.
19. A. Cuervo, M. Pulido-Cid, M. Chagoyen, R. Arranz, V. A. Gonzalez-Garca, C. Garcia-Doval, J. R. Castón, J. M. Valpuesta, M. J. van Raaij, J. Martín-Benito and J. L. Carrascosa, *Journal of Biological Chemistry*, 2013, **288**, 26290-26299.
20. X. Agirrezabala, J. A. Velazquez-Muriel, P. Gomez-Puertas, S. H. W. Scheres, J. M. Carazo and J. L. Carrascosa, *Structure*, 2007, **15**, 461-472.
21. O. D. Monera, C. M. Kay and R. S. Hodges, *Protein Sci.*, 1994, **3**, 1984-1991.
22. R. Zangi, R. H. Zhou and B. J. Berne, *J. Am. Chem. Soc.*, 2009, **131**, 1535-1541.
23. J. L. England and G. Haran, *Annual Review of Physical Chemistry, Vol 62*, 2011, **62**, 257-277.

24. J. P. Michel, I. L. Ivanovska, M. M. Gibbons, W. S. Klug, C. M. Knobler, G. J. L. Wuite and C. F. Schmidt, *Proc. Natl. Acad. Sci. U. S. A.*, 2006, **103**, 6184-6189.
25. M. M. Gibbons and W. S. Klug, *Biophys. J.*, 2008, **95**, 3640-3649.
26. A. Ionel, J. A. Velazquez-Muriel, D. Luque, A. Cuervo, J. R. Caston, J. M. Valpuesta, J. Martin-Benito and J. L. Carrascosa, *J. Biol. Chem.*, 2011, **286**, 234-242.
27. G. A. Vliegenthart and G. Gompper, *Biophysical Journal*, 2006, **91**, 834-841.
28. R. Zandi and D. Reguera, *Phys Rev E*, 2005, **72**, 21917.
29. M. Aznar, A. Luque and D. Reguera, *Physical Biology*, 2012, **9**.
30. J. Schijve, *Fatigue of Structures and Materials*, Kluwer Academic Publishers, Dordrecht, 2009.
31. A. Ortega-Esteban, A. J. Pérez-Berná, R. Menéndez-Conejero, S. J. Flint, C. San Martín and P. J. de Pablo, *Sci. Rep.*, 2013, **3**, 1434.
32. I. L. Ivanovska, R. Miranda, J. L. Carrascosa, G. J. L. Wuite and C. F. Schmidt, *Proc. Natl. Acad. Sci. U. S. A.*, 2011, **108**, 12611-12616.
33. J. S. Villarrubia, *J Res Natl Inst Stan*, 1997, **102**, 425-454.
34. I. Horcas, R. Fernandez, J. M. Gomez-Rodriguez, J. Colchero, J. Gomez-Herrero and A. M. Baro, *Rev. Sci. Instrum.*, 2007, **78**, 013705.
35. M. Buenemann and P. Lenz, *Proceedings of the National Academy of Sciences of the United States of America*, 2007, **104**, 9925-9930.
36. F. Moreno-Herrero, P. J. de Pablo, M. Alvarez, J. Colchero, J. Gomez-Hertero and A. M. Baro, *Appl. Surf. Sci.*, 2003, **210**, 22-26.
37. J. E. Sader, J. W. M. Chon and P. Mulvaney, *Rev. Sci. Instrum.*, 1999, **70**, 3967-3969.
38. M. Zink and H. Grubmuller, *Biophys. J.*, 2009, **96**, 1350-1363.
39. P. J. de Pablo, I. A. T. Schaap, F. C. MacKintosh and C. F. Schmidt, *Phys. Rev. Lett.*, 2003, **91**, 98101.

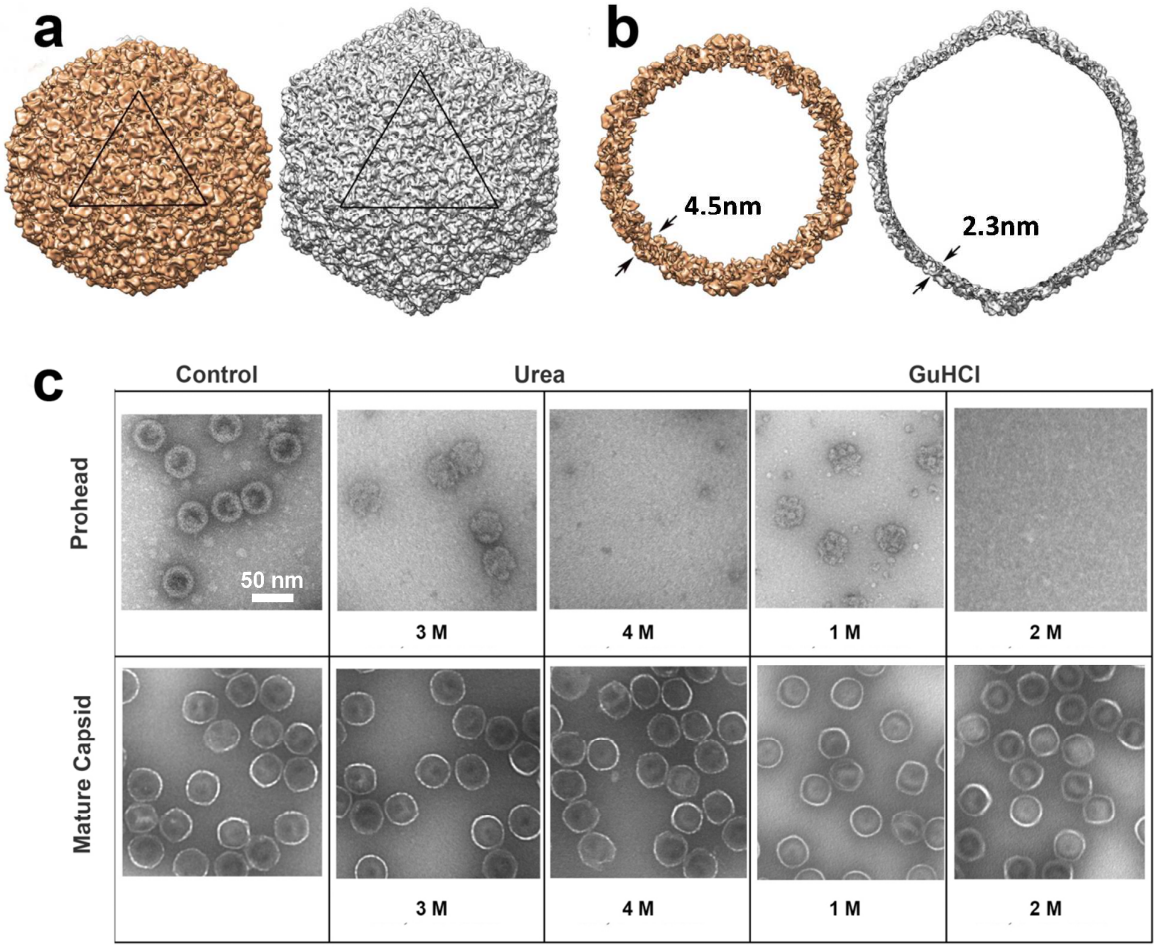

Fig 1. Maturation and chemical stability. (a) Structural changes produced during maturation and (b) comparison between the cross-sections of the cryoEM derived volumes of proheads (orange) and capsids (grey)[26]. (c) Comparison of the integrity of proheads and empty mature capsids under different concentrations of urea and GuHCl, as indicated (final concentrations). Samples were incubated for 20 min at 37º C, negatively stained and observed by electron microscopy. Scale bar represents 50 nm. The magnification is the same for all images.

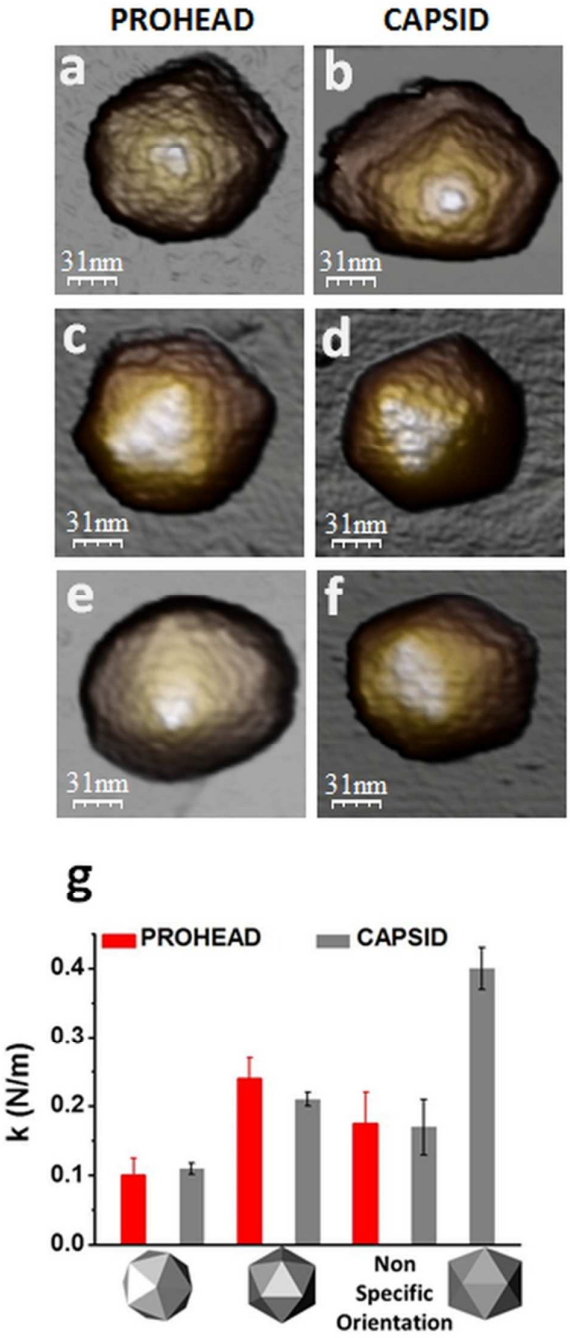

Fig 2. AFM topographies and stiffness of bacteriophage T7 particles. (a) Prohead adsorbed on a 5-fold symmetry axis. (b) Capsid absorbed on a 5-fold symmetry axis. (c) Prohead adsorbed on a triangular facet. (d) Capsid showing a three-fold symmetry axis. (e) Prohead adsorbed in a non-specific orientation. (f) Capsid adsorbed on a two-fold symmetry axis. (g) Stiffness data corresponding to 5-fold, and 3-fold symmetry axes, and non-specific orientations for proheads (red) and empty capsids (grey). The data corresponding to indentations on a two-fold axis is only depicted for capsids.

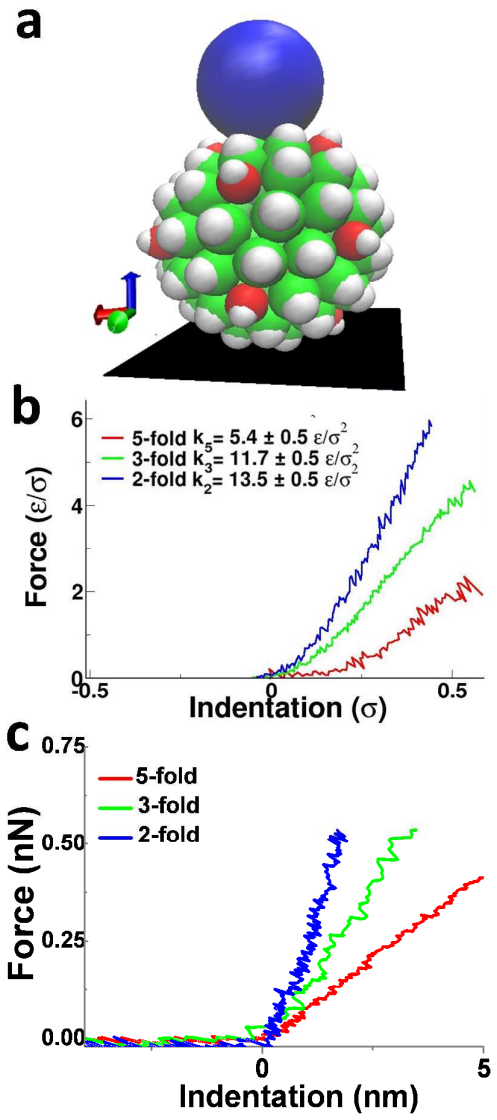

Fig 3. Anisotropic elasticity of capsids: (a) Snapshot of the indentation of a T7 coarse-grained model along the 2-fold direction. The blue sphere represents the AFM tip. The T7 capsid is modeled at the level of capsomers, where hexons and pentons are represented by green and red spheres, respectively. The small white spheres indicate the orientation of the capsomers. (b) Force exerted by the tip as a function of indentation, when the model capsid is indented along the different orientations: 5-fold (red), 3-fold (green) and 2-fold (blue). The slope of a linear fit of each curve yields the values of the effective spring constants indicated in the legend. Forces, indentations, and slopes are reported in scaled units in terms of σ (the diameter of the capsomers) and ε (the binding strength between capsomers) (c) Experimental nanoindentation curves peformed on capsid adsorbed on 5-fold (red), 3-fold (green) and 2-fold (blue) symmetry axes.

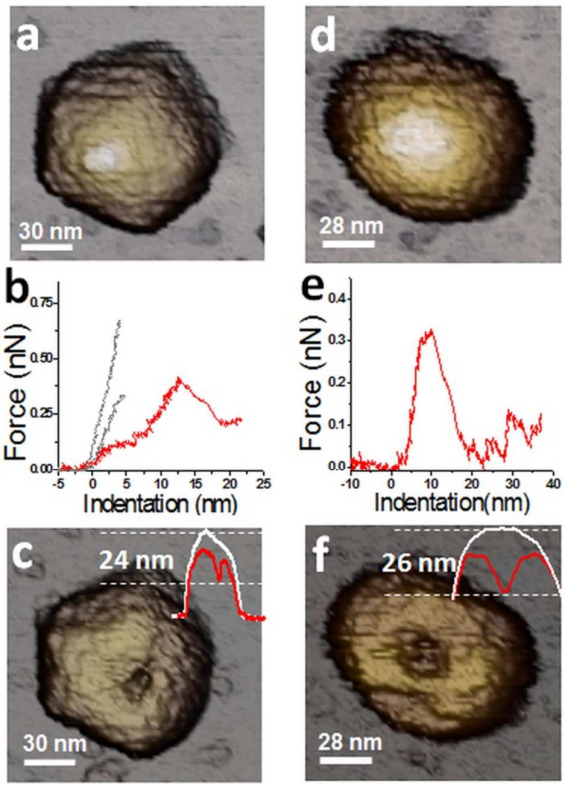

Fig 4. Mechanical fatigue and fracture of T7 proheads. (a) AFM topography image before mechanical fatigue of a prohead particle absorbed on 5-fold symmetry axes. (b) Three nanoindentation cycles performed on (a). The third curve (red) fractured the prohead. (c) Fractured prohead. The inset shows a comparison of the profiles along the damaged area before (white) and after (red) fracture. (d) (e) and (f) show the same sequence as (a), (b) and (c) for another prohead example absorbed on NSO, although in this case the particle fractured after only one cycle

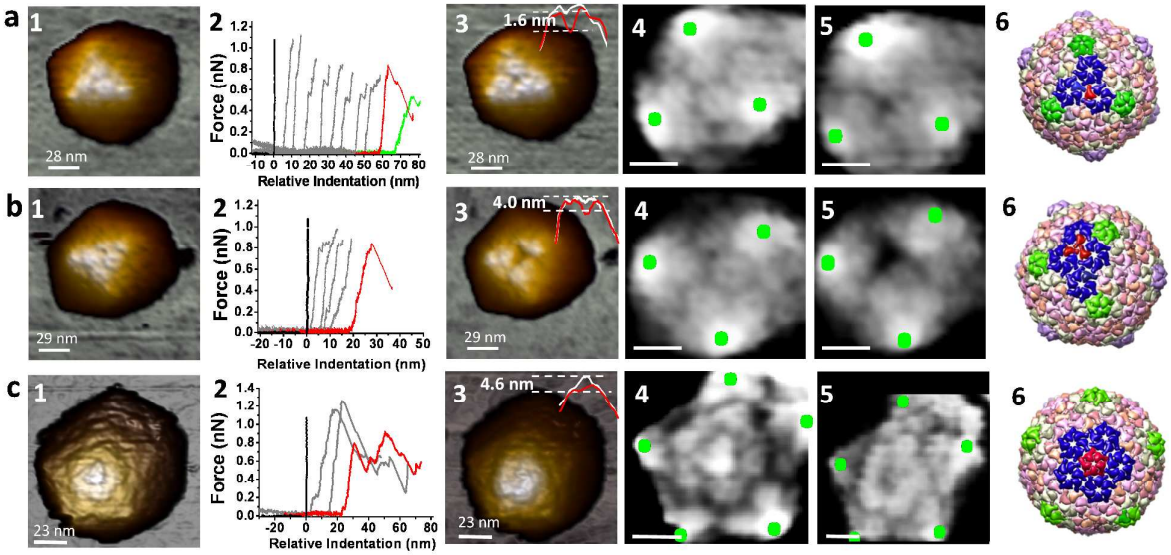

Fig 5. Mechanical fatigue and fracture of T7 mature capsids. (a1) Capsid adsorbed along a three-fold symmetry axis before mechanical fracture. (a2) Nanoindentation cycles performed on the particle shown in a1, shifted in the horizontal axis for ~~clarity~~ showing the temporal evolution. The black curve relates the nanoindentation on substrate. The red curve damaged the capsid, (green curve after damage). (a3) Damaged capsid. The inset shows a comparison of the profiles along the damaged area before (white) and after (red) fracture. Filtered topography before (a4), and after fracture (a5). The green dots help for correct identification of the fractures, and the scale bars indicate the same distance as topographies. (a6) Interpretation of the fractured particle on the cryo-EM derived model (pentons depicted in green, hexons in blue) indicating in red the subunits involved in the fracture (monomer). (b) Same description as (a), showing the fracture of a trimer of the particle adsorbed on three-fold symmetry axis. (c) Same description as (a), showing the fracture of a penton of the particle adsorbed on five-fold symmetry axis

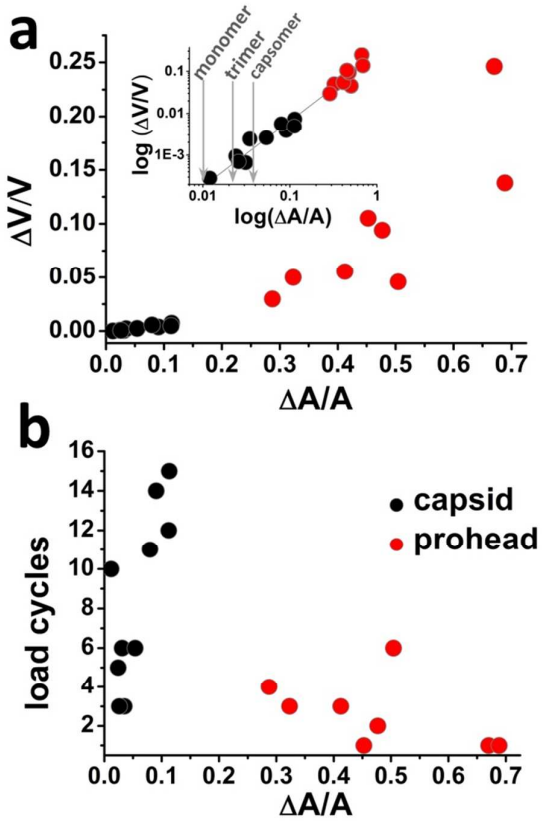

Fig 6. Fragility of proheads and capsids. (a) Chart of the normalized losses of volume (ΔV) and area (ΔA) produced by the fracture in proheads (red) and capsids (black). (inset, a) Log-log plot of the data shown in (a), where the slope of the linear fit is 1.57± 0.6. Grey arrows point to the normalized area corresponding to a monomer, a trimer and a pentamer, respectively. (b) Graph of the normalized damaged area for each particle vs. the number of load cycles required to produce it.

	K_5 (N/m)	K_3(N/m)	K_2 (N/m)	K_{NSO} (N/m)	# particles	#FvZ
Prohead	0.10 ± 0.02	0.24 ± 0.04	----------	0.17 ± 0.04	25	137
Capsid	0.11 ± 0.02	0.21 ± 0.03	0.40 ±0.02	0.17 ± 0.04	41	219

Table 1: **Summary of elastic constants**. Elastic constants measured for the T7 prohead and capsid for the different symmetries. The reported error is the standard deviation of the mean.